Colloids and Surfaces B: Biointerfaces 245 (2025) 114209

Contents lists available at ScienceDirect

Colloids and Surfaces B: Biointerfaces

journal homepage: www.elsevier.com/locate/colsurfb

Enzymeless detection and real-time analysis of intracellular hydrogen peroxide released from cancer cells using gold nanoparticles embedded bimetallic metal organic framework

K Theyagarajan [a,b], Buddolla Anantha Lakshmi [a,b], Young-Joon Kim [a,b,*]

[a] Department of Electronic Engineering, Gachon University, Seongnam 13120, Republic of Korea
[b] Department of Semiconductor Engineering, Gachon University, Seongnam 13120, Republic of Korea

ARTICLE INFO

Keywords:
Hydrogen peroxide
Electrochemical sensor
Modified electrode
Electrocatalyst
Metal organic framework
HeLa cells

ABSTRACT

Abnormal cell growth and proliferation can lead to tumor formation and cancer, one of the most fatal diseases worldwide. Hydrogen peroxide (H_2O_2) has emerged as a cancer biomarker, with its concentration being crucial for distinguishing cancer cells from normal cells. Herein, a cost-effective and enzymeless electrochemical sensing system for the monitoring of intracellular H_2O_2 has been constructed. The sensor is fabricated using gold nanoparticles embedded bimetallic copper/nickel metal organic framework (Au-CNMOF) immobilized reduced graphene oxide (RGO) modified screen printed electrode (SPE). The synthesized materials were characterized and confirmed by XRD, FTIR, SEM with EDS, and electrochemical analysis. The fabricated sensor displayed a redox peak at a formal potential (E°) of −0.155 V, corresponding to $Cu^{II/I}$ redox couple of CNMOF in 0.1 M phosphate buffer. Electrochemical investigations revealed that the proposed sensor has a large electrochemical active surface area (1.113 cm^2) and a higher surface roughness (5.67). Additionally, the sensor demonstrated excellent electrocatalytic activity towards H_2O_2 at −0.3 V, over a wide linear detection range from 28.5 μM to 4.564 mM with a limit of detection of 4.2 μM (S/N=3). Furthermore, the proposed sensor exhibits excellent stability, repeatability, reproducibility, and good anti-interference activity. Ultimately, the sensor was validated through real-time analysis of H_2O_2 released from cancer cells, successfully quantifying the released H_2O_2. The developed sensor holds great promise for real-time H_2O_2 analysis, with potential applications in clinical diagnostics, biological research and environmental monitoring.

1. Introduction

Designing a highly sensitive hydrogen peroxide (H_2O_2) sensor is crucial in clinical, biological, industrial, and environmental monitoring due to its significant role in various applications [1,2]·H_2O_2 is a versatile chemical and an essential biomarker, playing a critical role in the normal functioning and proliferation of cells [3,4]. However, abnormal secretion and accumulation of H_2O_2 indicate excessive oxidative stress and may be associated with various pathological conditions such as Alzheimer's disease, Parkinson's disease, cardiac disorders, diabetes and cancer [5,6]. The average H_2O_2 concentration in the blood ranges from 1 to 5 μM but during inflammation, it can increase to 30–50 μM. Moreover, the high concentrations of H_2O_2 exhibited by cancer cells can initiate tumor formation and contribute to tumor progression and metastasis. Due to aberrant metabolism, H_2O_2 is often overproduced in the tumor cells, making it a potential diagnostic tool for cancer [7]. Therefore, accurately measuring the concentration of H_2O_2 in the cellular environment provides valuable information for clinical diagnosis, biomedical research, drug discovery, and delivery [8,9]. Among the various analytical techniques developed for the selective sensing of H_2O_2, electrochemical sensing techniques have garnered significant interest due to their superior properties such as rapid response, high sensitivity, good selectivity, operational comfort, cost efficiency, portability, miniaturization capability, and applicability in continuous and on-site monitoring [10–13]. As a result, electrochemical sensors and biosensors have been extensively explored and are being utilized in the development of portable, continuous monitoring, and wearable sensing devices.

Designing a highly robust and cost-effective electrocatalyst is a challenging aspect of constructing novel electrochemical sensors. To

* Corresponding author at: Department of Electronic Engineering, Gachon University, Seongnam 13120, Republic of Korea
E-mail address: youngkim@gachon.ac.kr (Y.-J. Kim).

https://doi.org/10.1016/j.colsurfb.2024.114209

Available online 4 September 2024

date, various materials and molecules have been explored as electrocatalysts, ranging from carbon nanomaterials, metal nanoparticles, and organic frameworks to 0-3D materials, ionic liquids, nanozymes, conducting polymers, and dendrimers [14–17]. Among these, metal-organic frameworks (MOFs) have been extensively studied for various electrochemical applications due to their large surface area, tunable porosity, large number of catalytically active sites, synthetic versatility, and good stability [18–21]. MOFs are porous crystalline compounds composed of metal ions or clusters coordinated to organic linkers, forming 1–3D structures. Moreover, MOFs are cost-effective, environmentally friendly, easy to synthesize, can be sustainably produced in bulk quantities, and are highly suitable for large-scale industrial applications [22–25]. However, MOF-based electrocatalysts often face limited applications due to poor conductivity and reduced catalytic activity. To address these issues, various methods have been employed, such as functionalization, doping, intercalation, composite formation, polymer coating, defect engineering, and surface modification [26–29]. For instance, copolymer-based MOF hybrids consisting of polyaniline, polyanthranilic acid and UiO-66-NH_2 MOF [30], a nitrogen-enriched Co-MOF [31] and iron oxide supported MIL-101(Fe) MOF [32] were developed and utilized for the ultrasensitive detection of H_2O_2. These attempts were made to improve the conductivity, catalytic activity, mass transport and stability of the MOF-based electrocatalysts. Additionally, multi-metallic MOFs offer better stability and enhanced catalytic activity compared to mono-metallic MOFs [33]. For instance, a nitrogen doped CNT integrated cobalt/copper bimetallic MOF was employed for the ultrasensitive detection of H_2O_2 [34]. Therefore, developing a high performing electrocatalyst using cost-effective, scalable MOFs would open new avenues in the field of electrochemical sensors.

With this background, we designed a bimetallic copper/nickel MOF (CNMOF) and strategically utilized its pores for the stable anchoring of AuNPs, resulting in the desired Au-CNMOF hybrid. The hybrid was then immobilized over an electrochemically reduced graphene oxide network to improve the conductivity and stability of the fabricated sensor. Due to the incorporation of AuNPs, CNMOF, and RGO, the proposed sensor offers several advantages such as large surface area, excellent electron transport properties, and a greater number of catalytically active sites. Moreover, the sensor demonstrated excellent electrocatalytic activity, outstanding operational stability, good reproducibility, and remarkable selectivity towards H_2O_2. This significant performance is accredited to the effective incorporation of AuNPs into the porous structure of CNMOF, which efficiently augmented the electrochemical and electrocatalytic properties of the designed sensor. Moreover, the sensor was successfully employed for the monitoring of intracellular H_2O_2 released from HeLa cells. These results indicate that the proposed sensor could be applied for the diagnosis of various medical conditions like cancer, heart disease and so forth.

2. Experimental methods

2.1. Materials and instrumentation methods

Benzene-1,3,5-tricarboxylic acid (95%), copper(II) nitrate trihydrate (99–104%), nickel(II) nitrate hexahydrate (≥97%), hydrogen peroxide solution (30% w/w), dihydroethidium (≥95%) and gold nanoparticles (dia. 20 nm) were purchased from Sigma Aldrich, Korea. The cervical cancer (HeLa) cell line was purchased from the American Type Culture Collection, USA. All other reagents used were of analytical grade and used as received without further purification. Screen printed single electrodes (SPE) with a geometric area of 0.196 cm^2 were obtained from Zensor, Taiwan and used as the working electrode. The aqueous Ag/AgCl electrode (reference) was obtained from CH Instruments, Austin, and the platinum coil (counter electrode) was purchased from BASi, USA. Fourier transform infrared (FTIR) spectroscopy was performed in a JASCO FT/IR-4600 spectrophotometer. Powder X-ray diffraction (XRD) patterns were obtained from the Rigaku Ultima III X-ray diffractometer. Scanning electron microscope (SEM) images were acquired from the Hitachi SU8600 with a cold cathode field emission electron gun. For EDS analysis, the samples were coated with a mixture of palladium and platinum. All the electrochemical experiments were carried out in IVIUM CompactStat.h potentiostat, Netherlands. The fluorescence microscopic images were acquired from the EVOS M5000 imaging system, Thermo Fisher Scientific, USA. The aqueous solutions were prepared with Milli-Q water (18.2 MΩ cm) obtained from the Merck Millipore water system.

2.2. Synthesis of CNMOF

The synthesis of the copper-nickel metal organic framework (CNMOF) was carried out by following a literature procedure [35]. First, 4 mM of benzene-1,3,5-tricarboxylic acid was dissolved in methanol, to which 3.5 mM of each copper nitrate and nickel nitrate, also dissolved in methanol, was added. The resulting solution was constantly stirred at room temperature (RT) for about 24 h. Thereafter, the reaction mixture was washed with methanol and milli-Q water by centrifugation, and the resulting solid was dried in a hot air oven at 60 °C for 12 h, yielding the CNMOF (Fig. 1). For comparison, CMOF (copper MOF) was prepared by following the same procedure without the addition of nickel nitrate.

2.3. Preparation of graphene oxide and Au-CNMOF dispersions

Graphene oxide (GO) was synthesized by following the modified Hummer's method reported earlier [36]. The GO dispersion was prepared by dispersing 1 mg of the synthesized GO in a Milli-Q water and dimethylformamide mixture (9:1) and sonicating in an ultrasonic bath for 5 h. On the other hand, Au-CNMOF dispersion was prepared by dispersing 3 mg of CNMOF in ethanol, Nafion and water mixture (35:3:2) until a uniform dispersion was achieved. To this, 200 μL of AuNPs were added and the entire solution was sonicated in an ultrasonic bath for 2 h, yielding the proposed Au-CNMOF. Similarly, the CNMOF (without AuNPs) ink solution was prepared by following the same protocol, with the volume of AuNPs replaced by Milli-Q water.

2.4. Fabrication of Au-CNMOF/RGO/SPE sensor

Initially, the SPE was anodized by applying a constant potential of +2.0 V for 500 s in 0.1 M phosphate buffer solution (PBS), then it was washed with Milli-Q water and dried in air. Subsequently, an optimized volume of 10 μL of GO suspension (Fig. S1A) was drop coated over the anodized SPE to form the GO/SPE. After drying at RT, GO was electrochemically reduced to RGO by performing cyclic voltammetry between the potential window of 0 and −1.5 V at 50 mV/s in 0.1 M PBS until stable current was obtained as shown in Fig. S2. Thereafter, an optimized volume of 8 μL of Au-CNMOF (Fig. S1B) was drop coated over the as prepared RGO/SPE and left it for drying at RT for 2 h (Fig. S1C) to obtain the desired Au-CNMOF/RGO/SPE sensor, as shown in Fig. 1. Similarly, CNMOF/RGO/SPE (without AuNPs) sensor also prepared for comparison.

3. Results and discussions

3.1. Material characterization

The synthesized materials were characterized using powder XRD, FTIR spectroscopy and SEM with EDS analysis. The XRD pattern of CMOF and CNMOF are shown in Fig. S3A. The CMOF (magenta curve) showed a well crystalline pattern with the characteristic peaks at 2θ values 6.66°, 9.43°, 11.62°, 13.42°, 14.61°, 15.04°, 16.47°, 17.45°, 19.02°, 20.21°, 21.33°, 23.34°, 24.08°, 25.95°, 27.68°, 29.34°, 35.19°, 39.12° corresponding to the reflection planes (200), (220), (222), (400), (331), (420), (422), (500), (440), (600), (620), (444), (551), (731), (822), (751), (773) and (882), respectively. Thus obtained patterns are

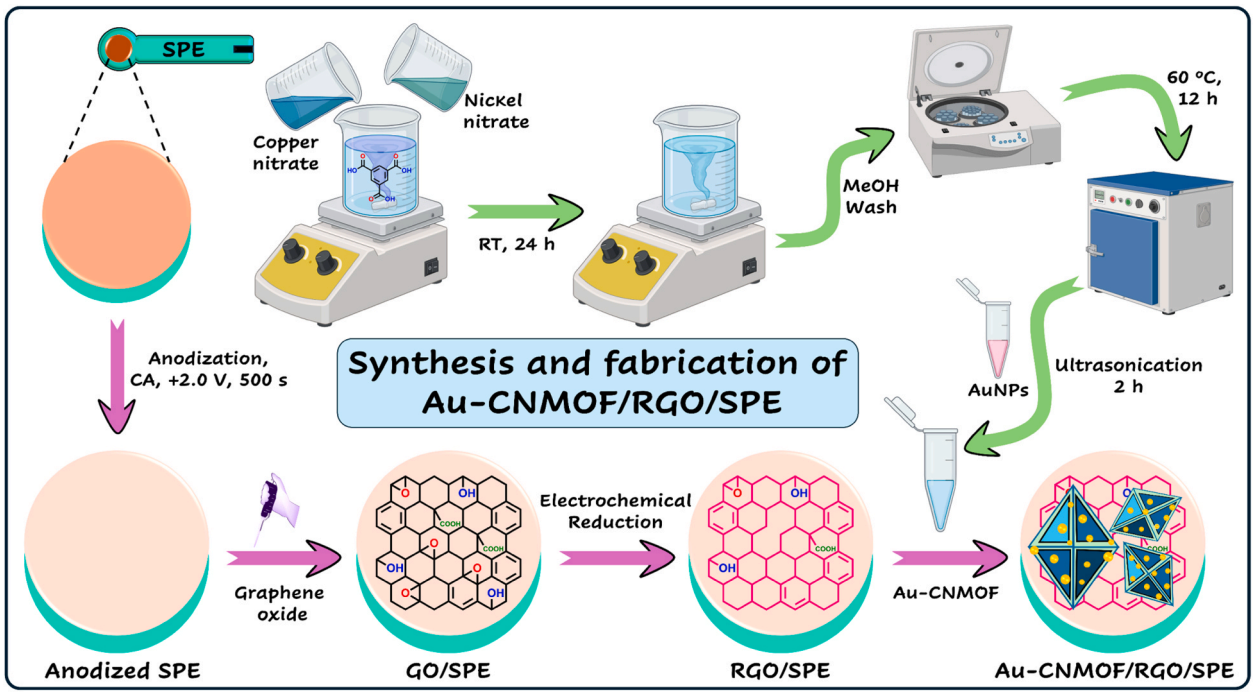

Fig. 1. Graphical illustration for the synthesis of Au-CNMOF and the fabrication of Au-CNMOF/RGO/SPE.

well-matched with the previous reports [37] and JCPDS no. 00–062–1183. The bimetallic CNMOF (blue curve) also exhibited a well-crystalline pattern with characteristic peaks mostly similar to that of CMOF with a slight variation in the peak intensities. This could be owing to the alike ionic radius of Ni^{2+} and Cu^{2+} in the CNMOF [35]. These results confirm that the successful formation of CMOF and CNMOF and the introduction of Ni into CMOF did not alter the crystallinity and phase purity of CNMOF. Besides, no other peaks related to any impurities were detected, signifying the high phase purity of the synthesized compounds. The presence of various functional groups in CMOF and CNMOF has been characterized by performing FTIR spectral analysis and the obtained spectra are shown in Fig. S3B. In the CMOF spectrum (magenta curve) the stretching vibration bands around 1629 and 1304 cm^{-1} were assigned to the asymmetric and symmetric stretching vibrations of C═O present in the MOF framework. Further, the peaks around 1435 and 1350 cm^{-1} corresponded to C═C and C-O stretching vibrations, respectively. The characteristic Cu-O (metal--organic ligand) stretching vibration appeared at 766 cm^{-1}, which confirms the formation of CMOF [38]. In the case of CNMOF (blue curve), all the stretching vibrations of CMOF appeared with slight differences in their intensities. Along with that, a new stretching vibration appeared around 549 and 690 cm^{-1} corresponding to the Ni-O stretching vibration, which confirms the formation of metal-oxo bond of Ni atoms with the carboxylate groups of BTC [39,40]. The powder XRD and FTIR results unambiguously confirmed the successful formation of CMOF and CNMOF.

Furthermore, SEM with EDS analysis was performed to identify the morphological characteristics and elemental composition of the synthesized compounds. The SEM image of CNMOF shows the octahedron morphology constituted with the well-defined eight triangular faces (Fig. 2A), which is similar to that of CMOF and consistent with previous reports [41,42]. Further, the chemical composition of the CNMOF was evaluated by EDS analysis and the overlaid EDS mapping of CNMOF is shown in Fig. S4. It confirms the presence of C, O, Cu and Ni elements in CNMOF structure, and the individual elemental mapping demonstrates the even distribution of all the elements. It is worth noting that the percentage of nickel is very low compared to copper. This could be due to the higher Lewis acidity and binding affinity of copper, which leads to most of the binding sites being occupied by Cu ions, with only a few sites occupied by Ni ions. The SEM image of Au-CNMOF also showed the octahedron morphology similar to that of CNMOF (Fig. 2B) without any significant changes. Moreover, the porous structure of CNMOF was maintained even after the formation of the Au-CNMOF hybrid, which reveals that ultrasonic-assisted processing did not alter the morphology of the parent material, and instead embedded the AuNPs in the pores of CNMOF. The overlaid EDS mapping of Au-CNMOF shows the presence of C, O, Cu, Ni and Au elements in the hybrid structure (Fig. 2C) and the individual mapping portrays the even distribution of the elements. Furthermore, the EDS spectrum and the composition analysis of Au-CNMOF are shown in Fig. S5. Besides, the EDS mapping of the Au-CNMOF hybrid clearly demonstrates the successful loading of AuNPs within the CNMOF matrix, indicating that the ultrasonication-assisted synthesis process effectively embedded the intended materials in the resulting hybrids. Therefore, XRD, FTIR and SEM with EDS analysis confirm the successful formation of CNMOF and Au-CNMOF hybrid.

3.2. *Electrochemical investigations on Au-CNMOF/RGO/SPE*

The fabricated sensor was characterized using various electrochemical techniques. Firstly, electrochemical impedance spectroscopy (EIS) was performed with different modified electrodes in 0.1 M KCl solution containing 5 mM of potassium ferrocyanide and ferricyanide. The EIS spectra have shown two regions, a semicircle at higher frequency region and a linear part at lower frequency region. The diameter of the semicircle directly denotes the charge transfer resistance (R_{ct}) of the designed probes, and Fig. 3 A shows the obtained EIS spectra of the various modified electrodes. The black curve represents the EIS of bare SPE, which showed an R_{ct} of 391 Ω due to the limited electron transfer at the bare SPE. After modifying with RGO, the R_{ct} reduced to 294 Ω, owing to the better electron transport properties of RGO. Further modifying with CNMOF, the CNMOF/RGO/SPE exhibited an R_{ct} of 183 Ω, which is lower than that of RGO/SPE and bare SPE. Finally, the introduction of AuNPs (Au-CNMOF/RGO/SPE) reduced the R_{ct} to the lowest value of 97 Ω, indicating the excellent electron transferability and low charge transfer resistance of the designed sensor. After that, cyclic voltammetry was carried out with all the modified electrodes

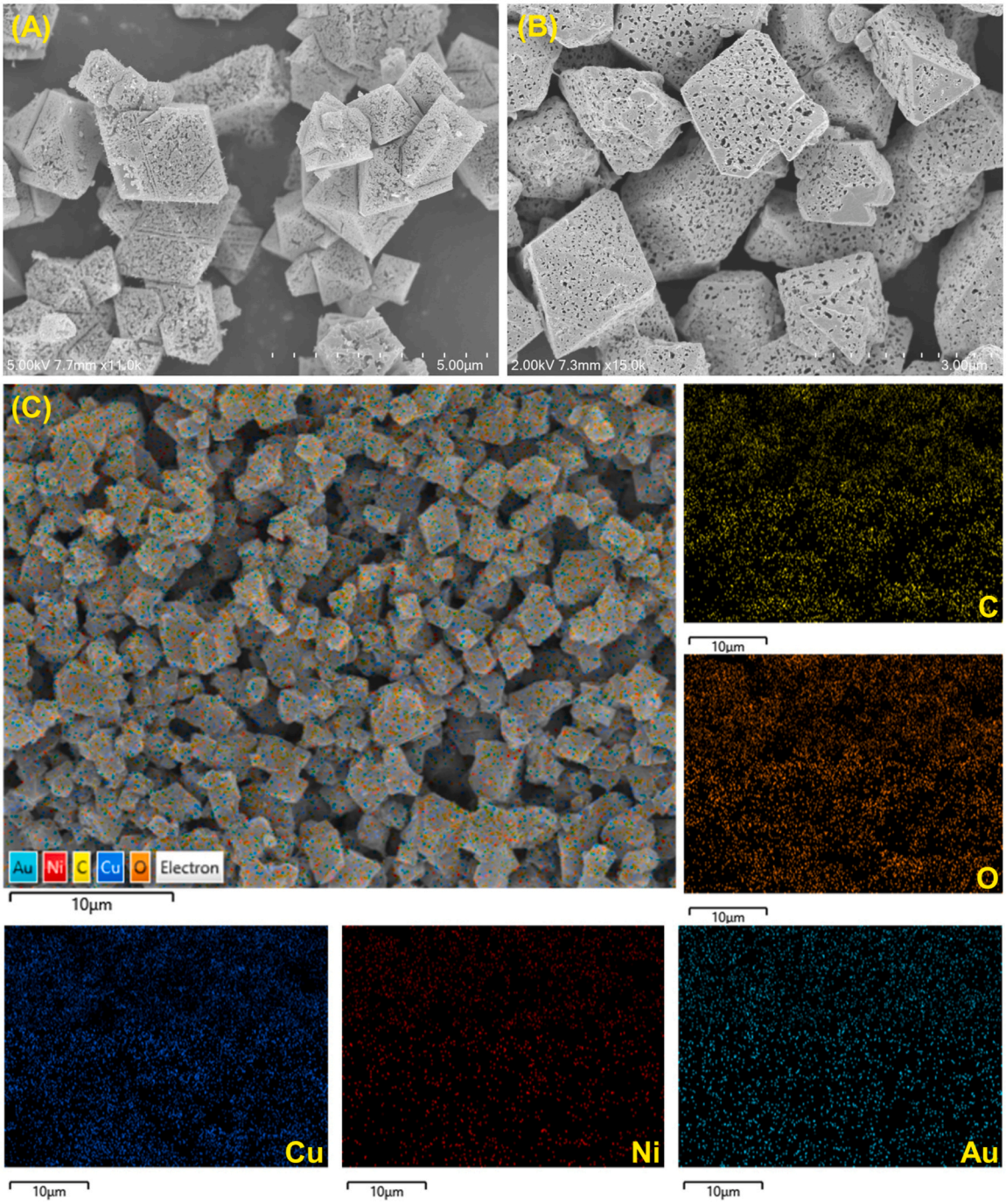

Fig. 2. SEM of (A) CNMOF and (B) Au-CNMOF. (C) Overlaid EDS mapping of Au-CNMOF and individual elemental mapping for C, O, Cu, Ni, and Au.

between the potential window of +0.3 V and −0.5 V in 0.1 M PBS (pH 7.2) at 50 mV s^{-1} and the obtained cyclic voltammograms (CVs) are displayed in Fig. 3B. The bare SPE (black curve) did not exhibit any observable redox peak denoting the absence of electroactive species. After RGO formation on SPE, the RGO/SPE (red curve) exhibited a capacitive behavior compared to bare SPE. The blue curve represents the CNMOF/RGO/SPE response, which showed an improved current response than bare SPE and RGO/SPE denoting the better electrochemical activity of CNMOF. After incorporation of AuNPs, the Au-CNMOF/RGO/SPE (green curve) showed a redox hump for $Cu^{II/I}$ at an anodic peak current (E_{pa}) of −0.105 V and cathodic peak current (E_{pc}) of −0.206 V with a formal potential (E°) of −0.155 V, present in the CNMOF [43]. The designed Au-CNMOF/RGO/SPE sensor exhibited ~1.5, ~3.4 and ~29.2 folds excess current response than CNMOF/RGO/SPE, RGO/SPE and bare SPE, respectively. The superior electrochemical properties of Au-CNMOF/RGO/SPE attributed to the effective integration of AuNPs, CNMOF and RGO into the sensor setup, which significantly augmented the electrochemical response.

Further, the effect of scanning rate was investigated to understand the nature of the electrochemical process and to evaluate the electrochemically active surface area (ECSA). For that, Au-CNMOF/RGO/SPE was subjected to sequential potential scans at varying scan rates from 20 to 300 mV/s in 0.1 M KCl containing 5 mM $Fe(CN_6)^{3-/4-}$ (Fig. S6A). It is evident that for every increment in the scan rate, there was a significant increase in the peak currents as well. As portrayed in Fig. S6B, a linear behavior was observed for the plot of the square root of the scan

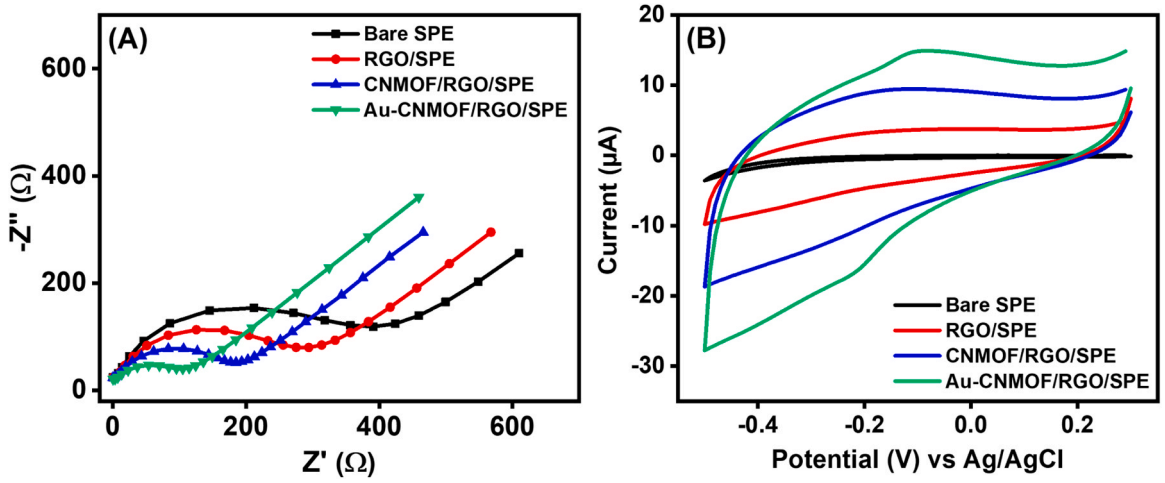

Fig. 3. (A) EIS in 0.1 M KCl containing 5 mM of $Fe(CN_6)^{3-/4-}$ and (B) CVs in 0.1 M PBS (pH 7.2) of Bare SPE (black), RGO/SPE (red), CNMOF/RGO/SPE (blue) and Au-CNMOF/RGO/SPE (green).

rate against peak currents, denoting a diffusion-controlled redox process at the developed sensor. In addition, the electrochemically active surface area of the fabricated sensor was calculated using the Randles-Sevcik equation (Fig. S7). It states that, in a reversible process, the peak current is directly proportional to the square root of the scan rate as shown in the Eq. (1).

$$I_p = (2.69 \times 10^5)\, n^{3/2}\, A\, D_o^{1/2}\, C_o\, \nu^{1/2} \quad (1)$$

Where I_p is the peak current in ampere, n is the number of electrons involved in the redox process, A is the electrochemical active surface area in cm^2, C_o is the concentration redox species in mol. cm^{-3}, ν is the scan rate in V s^{-1}, and D_o is the diffusion coefficient of the redox species (7.6×10^{-6} cm^2 s^{-1} for 5 mM of $[(Fe(CN)_6]^{3-/4-}$ at 25 °C) [44,45]. The ECSA was calculated to be 0.058, 0.193, 0.745 and 1.113 cm^2 for bare SPE, RGO/SPE, CNMOF/RGO/SPE and Au-CNMOF/RGO/SPE, respectively, which is ~19.1, ~5.7, ~1.5-folds higher than bare SPE, RGO/SPE, and CNMOF/RGO/SPE, respectively. Besides, the electrochemical roughness factor (R_f) was calculated for all the modified electrodes using the equation R_f = ECSA/GSA, where GSA is the geometric surface area of the electrode [46]. The roughness factor was calculated to be 0.29, 0.98, 3.80, and 5.67 for bare SPE, RGO/SPE, CNMOF/RGO/SPE, and Au-CNMOF/RGO/SPE, respectively. These superior properties could be attributed to several factors. The RGO layer provided enhanced electrochemical activity, increased surface area and porosity, improved electrical conductivity and stability, and facilitated the further immobilization of Au-CNMOF. Furthermore, the incorporation of CNMOF offered large internal porosity and high surface area, while the AuNPs contributed a large surface area and excellent electronic properties. Together, these components create an outstanding electrochemical sensing platform with an improved electrochemically

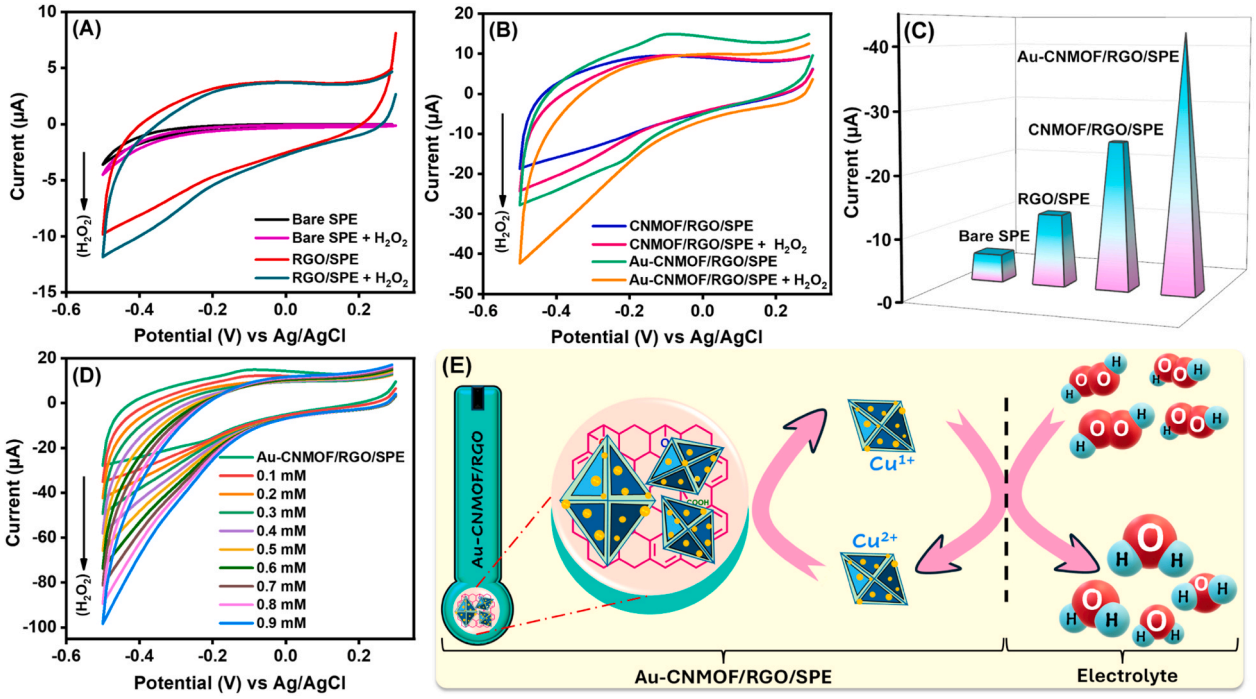

Fig. 4. (A) CVs of Bare SPE and RGO/SPE, (B) CNMOF/RGO/SPE and Au-CNMOF/RGO/SPE in the absence and presence of 0.2 mM H_2O_2. (C) Current response obtained for various modified electrodes for the reduction of 0.2 mM H_2O_2. (D) CVs of Au-CNMOF/RGO/SPE for the incremental concentrations of H_2O_2. Electrolyte: 0.1 M PBS (pH 7.2). (E) Mechanism for the electrochemical reduction of H_2O_2 at Au-CNMOF/RGO/SPE.

active surface area.

3.3. Electrocatalytic studies of Au-CNMOF/RGO/SPE towards H_2O_2

The prominent electrochemical performance of Au-CNMOF/RGO/SPE motivated us to explore its electrocatalytic properties towards H_2O_2. Fig. 4 A shows the electrocatalytic activities of bare SPE and RGO/SPE for the reduction of 0.2 mM of H_2O_2. It could be seen that bare SPE and RGO/SPE showed a feeble current response for H_2O_2 reduction in comparison with CNMOF/RGO/SPE and Au-CNMOF/RGO/SPE (Fig. 4B) for the same concentrations of H_2O_2. Besides, Au-CNMOF/RGO/SPE demonstrated ~1.7, 3.6, and 9.3 times (Fig. 4 C) better electrocatalytic response than CNMOF/RGO/SPE, RGO/SPE and bare SPE, respectively. Fig. 4D portrays the CVs of Au-CNMOF/RGO/SPE for the sequential additions of 0.1 mM of H_2O_2 and it is apparent that for every injection of H_2O_2, there was a linear increment in the reduction current. The sensing mechanism can be explained as follows: when a reducing potential is applied, the sensor is initially reduced and the reduced sensor reduces the diffusing H_2O_2 into water, causing the sensor to become oxidized (Fig. 4E). This cycle repeats until all the analytes present in the electrolyte are reduced. These results demonstrate the feasibility of the proposed sensor for H_2O_2 monitoring [47].

Further, to investigate the capability of the designed sensor under dynamic conditions, amperometry was performed at a fixed potential under constant stirring (300 rpm) in 0.1 M PBS. Initially, to determine the optimal potential for better performance, the Au-CNMOF/RGO/SPE was subjected to amperometry at various operating potentials ranging from 0 to −0.5 V for the reduction of 130 μM of H_2O_2 as shown in Fig. 5A. It could be observed that, as the applied potential increases, the corresponding response current also increased for the same concentrations of H_2O_2. When compared to −0.3, −0.4 and −0.5 V, the catalytic current responses are significantly lower at applied potentials 0, −0.1 and −0.2 V as shown in Fig. 5B. Although the amperometric responses at −0.3 and −0.4 V showed lower current than −0.5 V, the signal-to-noise ratio was significantly better. The higher noise at −0.5 V could be due to several factors, including increased background currents, enhanced electrochemical noise, increased capacitive currents and solution resistance. Therefore, among the two (-0.3 & −0.4 V) applied potentials, −0.3 V was chosen as the optimal potential for further studies, as it is the lowest best operating potential for better sensitivity and selectivity [48]. Thereafter, the amperometric response of various modified electrodes was explored at −0.3 V (Fig. 5C) for the same concentrations of H_2O_2. As shown in Fig. 5D, the Au-CNMOF/RGO/SPE showed better electrocatalytic response than CNMOF/RGO/SPE, RGO/SPE and bare SPE. The enhanced performance of Au-CNMOF/RGO/SPE could be ascribed to the efficient integration of AuNPs, CNMOF and RGO in the sensor fabrication, which synergistically augmented the electrochemical and electrocatalytic properties towards H_2O_2 detection. Fig. 5E displays the amperometry of Au-CNMOF/RGO/SPE at −0.3 V in 0.1 M PBS (pH 7.2) under constant stirring (300 rpm) with various concentrations of H_2O_2. The developed sensor showed a rapid increase in catalytic current for every addition of H_2O_2 and stabilized within <5 seconds. The rapid current increase implies the excellent electrocatalytic reduction ability of the proposed sensor, and the increase is directly proportional to the concentration of H_2O_2 spiked into the PBS. Further, a plot of the concentration of H_2O_2 against the catalytic current was plotted (Fig. 5F) and it showed a linear detection range of 28.5 μM – 4.564 mM with a limit of detection and sensitivity of 4.2 μM (3σ/m) and 231.98 μA mM^{-1} cm^{-2}, respectively. Moreover, the obtained electroanalytical performance of the designed sensor is compared with various MOF-based non-enzymatic H_2O_2 sensors in terms of linear range, LOD, sensitivity, pH, and operating potential. It could be seen from Table 1 that the obtained performance is superior or comparable with the sensors reported in the literature.

3.4. Exploring the stability, reproducibility, repeatability, and selectivity of Au-CNMOF/RGO/SPE

After the successful evaluation of the electrocatalytic activities of the developed sensor, it is important to investigate its stability,

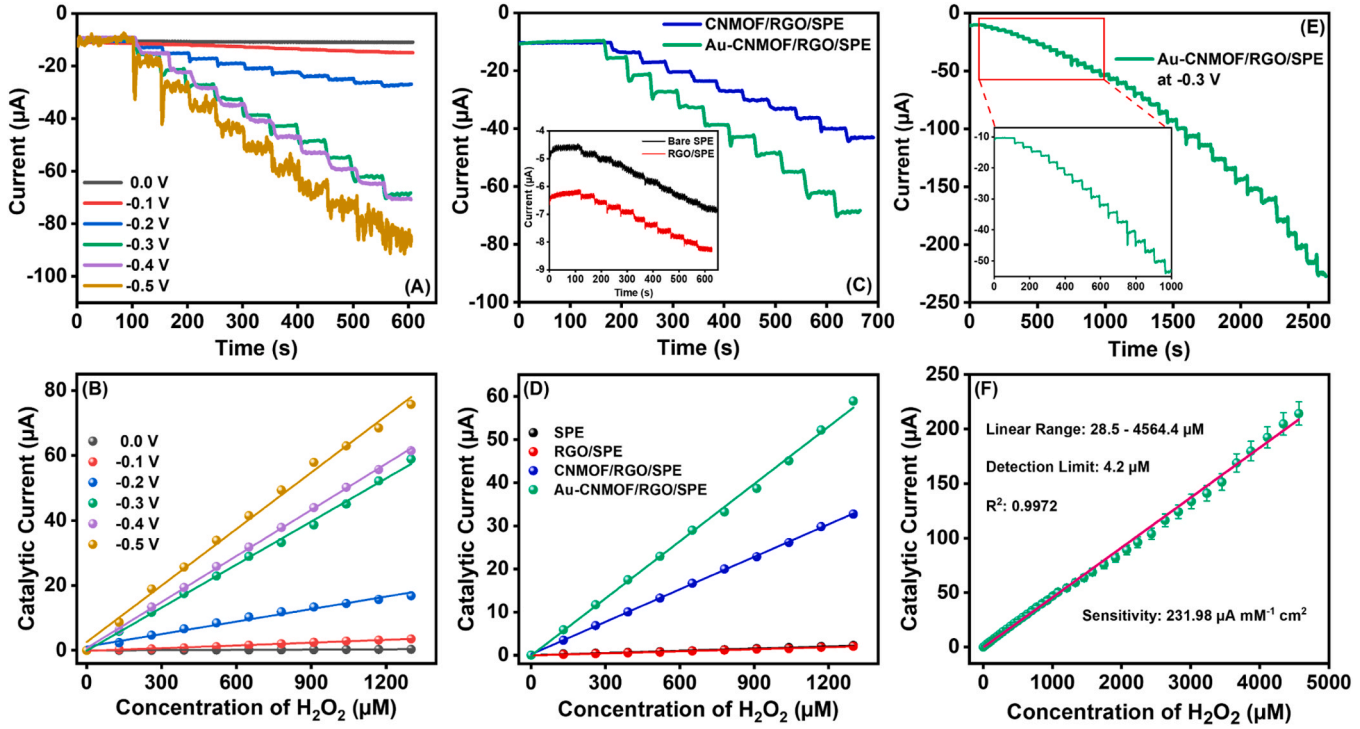

Fig. 5. Amperometric responses of (A) Au-CNMOF/RGO/SPE at different potentials, (C) Various modified electrodes at −0.3 V for the sequential additions of 130 μM of H_2O_2 (each) and (E) Au-CNMOF/RGO/SPE at −0.3 V for various concentrations of H_2O_2 (Inset: Selected area enlarged view of 0 – 1000 s). (B), (D) and (F) Corresponding calibration plots. Electrolyte: 0.1 M PBS (pH 7.2) under constant stirring (300 rpm).

Table 1
Comparison of electroanalytical performances of various MOF based H_2O_2 sensors.

Sensors	Linear range (μM)	LOD (μM)	Sensitivity (μA/mM/cm^2)	pH	Potential (V)	Ref.
AuNPs/N-GQDs/PMOF/GCE	5 – 1000	3.38	134.26	4.0	−0.3 V	[49]
2D-Co-MOF@Nf/PGE	5 – 1000	-	0.684*	7.0	+0.9 V	[50]
CytC/CS/Cu/ZIF−8/GCE	10 – 5200	3.7	-	7.0	−0.3 V	[51]
Ni-Co-MOF/GCE	0 – 7000	180	1.12	13	-	[52]
Cu-MOF/SPE	10 – 1000	4.1	-	7.2	+0.6 V	[53]
Cu-MOF/Hemin/GCE	10 – 5000	4.14	0.52	7.0	−0.7 V	[54]
Ru-Cu-MOF/GCE	10 – 5550	8.9	327.14	7.2	−0.2 V	[55]
MIL−53-Cr^{III}/GCE	25 – 500	3.52	167.6	13	-	[56]
ZnO@ZIF−8	20 – 11,550	3.0	4.47	7.0	+0.6 V	[57]
AgNPs/Cu-MOF/GCE	3.7 – 5800	1.2	21.6	7.2	−0.25 V	[58]
Ni-MOF/CNT/GCE	10 – 51,600	2.1	115.49	13	+0.5 V	[59]
Au-CNMOF/RGO/SPE	28.5 – 4564	4.2	231.98	7.2	−0.3 V	**This work**

* μA/mM; CNT – Carbon nanotube; CS – Chitosan; CytC – Cytochrome C; GCE – Glassy carbon electrode; Nf – Nafion; PGE – Pencil graphite electrode; PMOF – PEI functionalized metal organic framework; RGO – Reduced graphene oxide; SPE – Screen printed electrode; ZIF – Zeolitic imidazolate framework.

reproducibility, repeatability, and selectivity. The operational stability of the designed sensor was analyzed by performing amperometry under constant stirring at −0.3 V continuously for 3000 seconds in the absence and presence of 0.65 mM of H_2O_2 as shown in Fig. 6 A. It is evident from the results that the developed sensor exhibited excellent stability even under dynamic conditions for such a long period, which confirms that the designed sensor is highly stable. Further, the long-term storage stability was investigated by examining the same sensor for 30 days in the absence and presence of 0.5 mM H_2O_2. From Fig. 6B it is evident that the proposed sensor exhibited ~90% and ~86% of its initial response even after 30 days in the absence and presence of H_2O_2. Furthermore, the reproducibility of the sensor was investigated by evaluating 5 individually constructed sensors in the absence and presence of 0.5 mM H_2O_2. The obtained current responses are illustrated in the form of a columnar diagram (Fig. 6 C), and it showed a relative standard deviation (RSD) of 3.12% and 3.88% in the absence and presence of H_2O_2, respectively. These results show that the developed sensor has good electrode-to-electrode reproducibility. Additionally, the repeatability of the sensor was evaluated by performing ten repetitive measurements with the same sensor for measuring 0.5 mM of H_2O_2 and the obtained current responses are displayed in Fig. 6D. The current difference between the first and tenth measurements is ~2.18% and hence, the sensor retained ~97.82% of its first response. The superior repeatability of the developed sensor could be due to the effective integration of AuNPs and CNMOF on the ERGO/SPE surface which firmly holds the sensor components and augmented the electron transport, robustness and stability. Further, the selectivity of the sensor plays a major role in determining the practical applicability of the designed system. Hence, the selectivity of the sensor was evaluated by performing amperometry at −0.3 V with 0.6 mM of H_2O_2 and 1 mM of various interfering species such as glucose, bromate, ascorbic acid, iodate, uric acid, dopamine, L-dopa, cholesterol, paracetamol, sulfite, and acetylcholine. It could be seen from Fig. 6E that the developed sensor showed a response only for H_2O_2 addition and no significant change during the additions of interferents. It further confirms that Au-CNMOF/RGO/SPE is highly selective for H_2O_2.

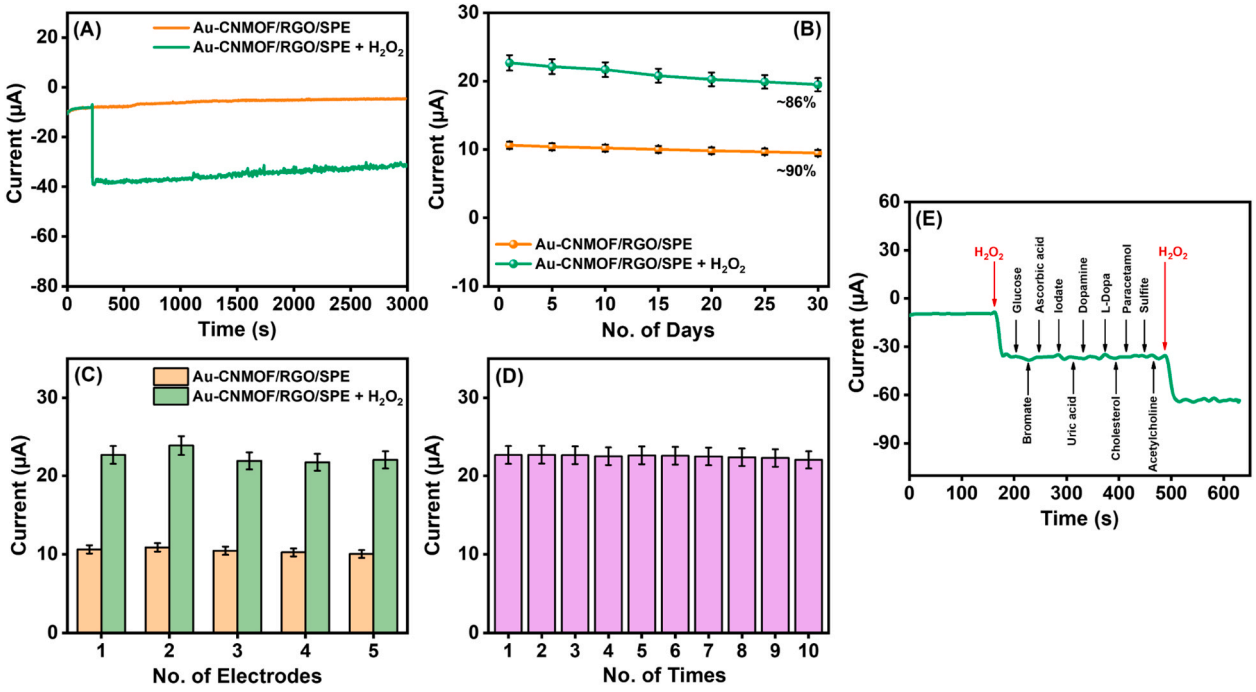

Fig. 6. (A) Amperometric response of Au-CNMOF/RGO/SPE for 3000 s in the absence and presence of 0.65 mM of H_2O_2 under constant stirring. (B) Long-term stability for 30 days and (C) Reproducibility of five different Au-CNMOF/RGO/SPE in the absence and presence of 0.5 mM H_2O_2. (D) Current response obtained for the 10 repetitive measurements using the same Au-CNMOF/RGO/SPE in the presence of 0.5 mM H_2O_2 (E) Amperometric response of Au-CNMOF/RGO/SPE towards 0.6 mM H_2O_2 in the presence of 1 mM concentrations of various interferents. Electrolyte: 0.1 M PBS (pH 7.2).

3.5. Real-time analysis of H_2O_2 released from HeLa cells

The excellent electroanalytical performance, including a long linear range, good operational stability, and selectivity of the designed Au-CNMOF/RGO/SPE sensor, motivated us to explore its practical applicability in the intracellular monitoring of H_2O_2. For this purpose, human cervical cancer cells (HeLa) were chosen as the model system, and ascorbic acid (AA) was utilized as the stimulating agent, which can induce the cells to release H_2O_2 within a short period [60,61]. The HeLa cells were cultivated in a 6-well plate, and their growth and proliferation were monitored using a fluorescence microscope. Fig. 7 A shows the microscopic image of HeLa cells, confirming that the spindle-shaped HeLa cells are well-grown and covering almost the entire area. Thereafter, the cells were rinsed twice to remove the media and other contaminants and filled with 0.1 M PBS (pH 7.2). To evaluate oxidative stress and superoxide release, the well-grown cells were stained with dihydroethidium (DHE) and examined under the fluorescence microscope. DHE is a DNA fluorescence dye and a highly specific indicator of superoxide anions [62]. When DHE is introduced into cells, it rapidly reacts with intracellular superoxide, producing a red fluorescent product called 2-hydroxyethidium. The scattered red dots in Fig. 7B show the superoxide release from the cells in their native state without any stimuli. Interestingly, after the injection of the stimuli (AA), the cells released larger quantities of H_2O_2, which is confirmed by the greater number of bright red spots in Fig. 7 C. The DHE fluorescence images proved that H_2O_2 release in HeLa cells is indeed stimulated by AA [63]. Furthermore, the cytotoxicity of Au-CNMOF towards NIH 3T3 and HeLa cells was evaluated using MTT assay. It is found that the synthesized Au-CNMOF is less toxic to 3T3 cells than HeLa cells (Fig. S8).

Thereafter, amperometry was performed at −0.3 V by immersing the sensor in the 6-well plate filled with PBS and HeLa cells. As shown in Fig. 7D, no change in the current response was observed for PBS + HeLa cells (red curve) in the absence of AA. Interestingly, upon the addition of the stimuli (1 mM) to the same solution, an immediate increase in the reduction current was observed (blue curve), which is ascribed to the reduction of H_2O_2 generated by the stimuli. Using the calibration plot, the quantity of H_2O_2 released from the cells was calculated to be 20 μM. In contrast, when the same amount of AA was added to the PBS (without cells), the background fluctuated slightly (black curve), and no apparent current change was observed. This further confirms that the current response is due to the reduction of H_2O_2 released from the HeLa cells and not from the stimuli. Furthermore, the sensor's long-term performance was investigated for a period of one week, which exhibited acceptable current response even after 7 days. The sensor was washed with PBS and stored dry when not in use. The graphical representation of in vitro detection and photograph of real-time analysis of H_2O_2 in HeLa cells are shown in Fig. 7E. These results confirm the potential applicability of the proposed sensor to monitor H_2O_2 release from living cells. The future development of enzymeless electrochemical H_2O_2 sensing systems holds great promise for clinical diagnostics, biological research, food analysis, industrial and environmental monitoring. To advance these systems, several key areas need to be addressed to enhance their sensitivity, selectivity, stability, and practicality. Further, integration of these sensors into portable, wearable or implantable devices can provide real-time monitoring of oxidative stress and other physiological parameters, offering valuable information for personalized medicine. Additionally, incorporating wireless communication technologies and Internet of Things (IoT) capabilities can facilitate remote monitoring and data transmission, making these sensors more versatile and convenient for users.

4. Conclusions

Herein, a cost-effective and disposable electrochemical sensing system for the detection of intracellular H_2O_2 was constructed using AuNPs, CNMOF and RGO. Initially, CNMOF was synthesized at room temperature, and AuNPs were ultrasonically embedded within the pores of CNMOF to form the Au-CNMOF hybrid. The hybrid was then immobilized onto the RGO-modified SPE to achieve the desired sensor. Electrochemical investigations revealed the sensor has low charge transfer resistance, a high electrochemically active surface area, and large surface roughness. These outstanding properties augmented the sensor's electrocatalytic activity, resulting in a wide linear detection range, good sensitivity, and selectivity, as well as excellent stability and reproducibility towards H_2O_2 detection. The superior performance could be attributed to the effective integration of AuNPs, CNMOF, and RGO, which accelerated the electron transport properties and increased the catalytically active sites. Furthermore, the developed sensor was

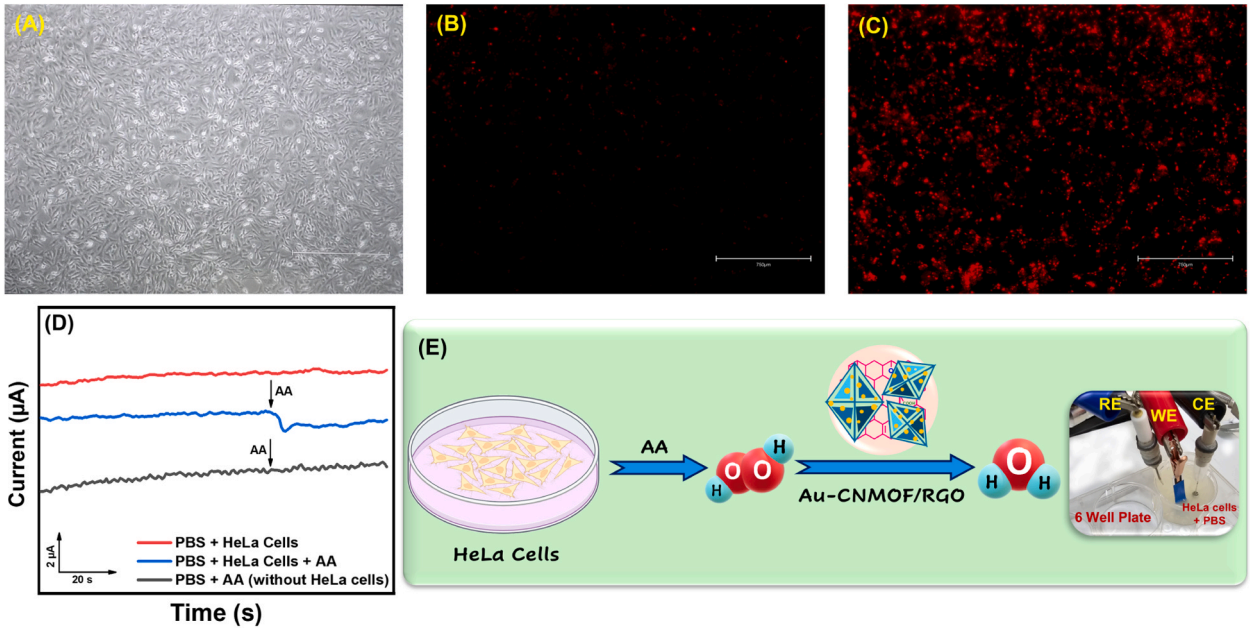

Fig. 7. (A) Microscopic image of proliferated HeLa cells. DHE fluorescence images of HeLa cells (B) without ascorbic acid and (C) with 1 mM ascorbic acid (D) Amperometric response of Au-CNMOF/RGO/SPE at −0.3 V in various conditions. (E) Scheme for the in vitro detection of H_2O_2 and photograph of real-time analysis.

successfully utilized for the real-time analysis of intracellular H_2O_2 released from HeLa cells. Unlike other sensors that require cells to be grown directly on the sensor surface, the advantage of the present method is that the sensor operates by being immersed in a cell solution without making any direct contact with the cells. This feature allows the sensor to be reused multiple times without any compromise in performance. However, a limitation of the proposed system is that it requires a concentrated volume of cells for the detection and quantification of H_2O_2 and further modifications are needed to achieve detection in the nanomolar range. These results confirm that the developed sensor holds great potential for application in cancer diagnosis, food analysis, and environmental monitoring.

CRediT authorship contribution statement

K Theyagarajan: Writing – review & editing, Writing – original draft, Visualization, Validation, Software, Resources, Methodology, Investigation, Formal analysis, Data curation, Conceptualization. **Buddolla Anantha Lakshmi:** Investigation, Formal analysis, Data curation. **Young-Joon Kim:** Writing – review & editing, Supervision, Resources, Project administration, Funding acquisition, Conceptualization.

Declaration of Competing Interest

The authors declare that they have no known competing financial interests or personal relationships that could have appeared to influence the work reported in this paper.

Data availability

Data will be made available on request.

Acknowledgments

This work was funded by the National Research Foundation of Korea (Grant number: NRF-2022R1F1A1074346 and RS-2024–00433166).

Appendix A. Supporting information

Supplementary data associated with this article can be found in the online version at doi:10.1016/j.colsurfb.2024.114209.

References

[1] R. Mandavkar, S. Lin, M.A. Habib, S. Burse, M.H. Joni, S. Kunwar, A. Najar, S. A. Aravindh, J.-H. Jeong, J. Lee, Ultra-sensitive H_2O_2 sensing with 3-D porous Au/CuO/Pt hybrid framework, Sens. Actuators B Chem. 396 (2023) 134512, https://doi.org/10.1016/j.snb.2023.134512.

[2] G. Zou, L. Sun, L. Huo, H. Zhao, Enzyme-free hydrogen peroxide sensing based on heterogeneous SnO_2@CuO/CF via interfacial engineering, Electrochim. Acta 487 (2024) 144163, https://doi.org/10.1016/j.electacta.2024.144163.

[3] Y. Yu, M. Pan, J. Peng, D. Hu, Y. Hao, Z. Qian, A review on recent advances in hydrogen peroxide electrochemical sensors for applications in cell detection, Chin. Chem. Lett. 33 (2022) 4133–4145, https://doi.org/10.1016/j.cclet.2022.02.045.

[4] X. Jin, C. Geng, D. Zhao, Y. Liu, X. Wang, X. Liu, D.K.Y. Wong, Peroxidase-encapsulated Zn/Co-zeolite imidazole framework nanosheets on ZnCoO nanowire array for detecting H_2O_2 derived from mitochondrial superoxide anion, Biosens. Bioelectron. 237 (2023) 115547, https://doi.org/10.1016/j.bios.2023.115547.

[5] J. Zheng, P. Zhao, S. Zhou, S. Chen, Y. Liang, F. Tian, J. Zhou, D. Huo, C. Hou, Development of Au–Pd@UiO-66-on-ZIF-L/CC as a self-supported electrochemical sensor for in situ monitoring of cellular hydrogen peroxide, J. Mater. Chem. B 9 (2021) 9031–9040, https://doi.org/10.1039/D1TB01120K.

[6] P. Arul, S.-T. Huang, V. Mani, C.-H. Huang, Gold–silver bimetallic alloy nanoparticles in a covalent organic framework for real-time monitoring of hydrogen peroxide from live cells, ACS Appl. Nano Mater. 5 (2022) 6340–6351, https://doi.org/10.1021/acsanm.2c00435.

[7] M.A. Riaz, Y. Chen, Electrodes and electrocatalysts for electrochemical hydrogen peroxide sensors: a review of design strategies, Nanoscale Horiz. 7 (2022) 463–479, https://doi.org/10.1039/D2NH00006G.

[8] F.X. Hu, J. Miao, C. Guo, H.B. Yang, B. Liu, Real-time photoelectrochemical quantification of hydrogen peroxide produced by living cells, Chem. Eng. J. 407 (2021) 127203, https://doi.org/10.1016/j.cej.2020.127203.

[9] J. Lu, Y. Hu, P. Wang, P. Liu, Z. Chen, D. Sun, Electrochemical biosensor based on gold nanoflowers-encapsulated magnetic metal-organic framework nanozymes for drug evaluation with in-situ monitoring of H_2O_2 released from H_9C_2 cardiac cells, Sens. Actuators B Chem. 311 (2020) 127909, https://doi.org/10.1016/j.snb.2020.127909.

[10] Z. Zeng, J. Wang, S. Zhao, Y. Zhang, J. Fan, H. Wu, J. Chen, Z. Zhang, Z. Meng, L. Yang, R. Wang, B. Zhang, G. Wang, C.-Z. Li, G. Zang, A bioinspired flexible sensor for electrochemical probing of dynamic redox disequilibrium in cancer cells, Adv. Sci. 10 (2023) 2304079, https://doi.org/10.1002/advs.202304079.

[11] Y. Li, L. Tang, D. Deng, J. Ye, Z. Wu, J. Wang, L. Luo, A novel non-enzymatic H_2O_2 sensor using ZnMn2O4 microspheres modified glassy carbon electrode, Colloids Surf. B Biointerfaces 179 (2019) 293–298, https://doi.org/10.1016/j.colsurfb.2019.04.008.

[12] X. Ding, F. Wang, H. Hu, S. Imhanria, W. Wang, J. Zhang, Tea-polyphenol green fabricating catkin-like CuAg for electrochemical H_2O_2 detection, Colloids Surf. B Biointerfaces 219 (2022) 112827, https://doi.org/10.1016/j.colsurfb.2022.112827.

[13] K. Theyagarajan, Y.-J. Kim, Recent Developments in the design and fabrication of electrochemical biosensors using functional materials and molecules, Biosensors 13 (2023) 424, https://doi.org/10.3390/bios13040424.

[14] T. Su, Z. Mi, Y. Xia, D. Jin, Q. Xu, X. Hu, Y. Shu, A wearable sweat electrochemical aptasensor based on the Ni–Co MOF nanosheet-decorated CNTs/PU film for monitoring of stress biomarker, Talanta 260 (2023) 124620, https://doi.org/10.1016/j.talanta.2023.124620.

[15] V.P. Sruthi, S. Senthilkumar, Prudently designed Se@fMWCNT as a peroxidase mimicking nanozyme for distinctive electrochemical detection of H_2O_2 and glutathione, J. Mater. Chem. C (2024), https://doi.org/10.1039/D4TC01231C.

[16] D. Mohanapriya, J. Satija, S. Senthilkumar, V. Kumar Ponnusamy, K. Thenmozhi, Design and engineering of 2D MXenes for point-of-care electrochemical detection of bioactive analytes and environmental pollutants, Coord. Chem. Rev. 507 (2024) 215746, https://doi.org/10.1016/j.ccr.2024.215746.

[17] Y. Jiang, X. Tong, Y. E, P. Wei, F. Fang, P. Chen, K. Qian, TiO_2-doped LTA zeolite as a sensitive non-enzymatic electrochemical sensor toward hydrogen peroxide detection, J. Alloy. Compd. 968 (2023) 171866, https://doi.org/10.1016/j.jallcom.2023.171866.

[18] M. Pan, H. Li, J. Yang, Y. Wang, Y. Wang, X. Han, S. Wang, Review: Synthesis of metal organic framework-based composites for application as immunosensors in food safety, Anal. Chim. Acta 1266 (2023) 341331, https://doi.org/10.1016/j.aca.2023.341331.

[19] R. Shubhangi, S.K. Kumari, P.Chandra Rai, Electrochemical assembly of nickel metal organic framework-decorated nanoimprinted gold dendrites as peroxidase mimic for high-performance hydrogen peroxide sensing, ACS Appl. Nano Mater. 7 (2024) 1388–1401, https://doi.org/10.1021/acsanm.3c05396.

[20] B. Mohan, D. Dhiman, Virender, Mehak, Priyanka, Q. Sun, M. Jan, G. Singh, N. Raghav, Metal-organic frameworks (MOFs) structural properties and electrochemical detection capability for cancer biomarkers, Microchem. J. 193 (2023) 108956, https://doi.org/10.1016/j.microc.2023.108956.

[21] A. Chaouiki, M. Chafiq, Y.G. Ko, The art of controlled nanoscale lattices: A review on the self-assembly of colloidal metal–organic framework particles and their multifaceted architectures, Mater. Sci. Eng. R. Rep. 159 (2024) 100785, https://doi.org/10.1016/j.mser.2024.100785.

[22] A. Das, S. Bej, N.R. Pandit, P. Banerjee, B. Biswas, Recent advancements of metal–organic frameworks in sensing platforms: relevance in the welfare of the environment and the medical sciences with regard to cancer and SARS-CoV-2, J. Mater. Chem. A 11 (2023) 6090–6128, https://doi.org/10.1039/D2TA07938K.

[23] K. Wang, X. Zheng, M. Qi, W. Zhang, J. Du, Q. Han, C. Li, B. Dong, L. Wang, L. Xu, Flexible screen-printed electrochemical platform to detect hydrogen peroxide for the indication of periodontal disease, Sens. Actuators B Chem. 390 (2023) 133955, https://doi.org/10.1016/j.snb.2023.133955.

[24] B. Mohan, S. Kumar, V. Kumar, T. Jiao, H.K. Sharma, Q. Chen, Electrochemiluminescence metal-organic frameworks biosensing materials for detecting cancer biomarkers, Trends Anal. Chem. 157 (2022) 116735, https://doi.org/10.1016/j.trac.2022.116735.

[25] B. Chen, Z. Yang, Q. Jia, R.J. Ball, Y. Zhu, Y. Xia, Emerging applications of metal-organic frameworks and derivatives in solar cells: recent advances and challenges, Mater. Sci. Eng. R. Rep. 152 (2023) 100714, https://doi.org/10.1016/j.mser.2022.100714.

[26] J.M. Gonçalves, P.R. Martins, D.P. Rocha, T.A. Matias, M.S.S. Julião, R.A. A. Munoz, L. Angnes, Recent trends and perspectives in electrochemical sensors based on MOF-derived materials, J. Mater. Chem. C 9 (2021) 8718–8745, https://doi.org/10.1039/D1TC02025K.

[27] S. Ma, S. Xiao, Y. Hong, Y. Bao, Z. Xu, D. Chen, X. Huang, Coupling metal organic frameworks nanozyme with carbon nanotubes on the gradient porous hollow fiber membrane for nonenzymatic electrochemical H_2O_2 detection, Anal. Chim. Acta 1293 (2024) 342285, https://doi.org/10.1016/j.aca.2024.342285.

[28] B. Mohan, Virender, R.K. Gupta, A.J.L. Pombeiro, A.A. Solovev, G. Singh, Advancements in metal-organic, enzymatic, and nanocomposite platforms for wireless sensors of the next generation, Adv. Funct. Mater. (2024) 2405231, https://doi.org/10.1002/adfm.202405231.

[29] B. Mohan, S. Kumar, H. Xi, S. Ma, Z. Tao, T. Xing, H. You, Y. Zhang, P. Ren, Fabricated metal-organic frameworks (MOFs) as luminescent and electrochemical biosensors for cancer biomarkers detection, Biosens. Bioelectron. 197 (2022) 113738, https://doi.org/10.1016/j.bios.2021.113738.

[30] S.A. Hira, M. Nallal, K. Rajendran, S. Song, S. Park, J.-M. Lee, S.H. Joo, K.H. Park, Ultrasensitive detection of hydrogen peroxide and dopamine using copolymer-

grafted metal-organic framework based electrochemical sensor, Anal. Chim. Acta 1118 (2020) 26–35, https://doi.org/10.1016/j.aca.2020.04.043.
[31] S.A. Hira, D. Annas, S. Nagappan, Y.A. Kumar, S. Song, H.-J. Kim, S. Park, K. H. Park, Electrochemical sensor based on nitrogen-enriched metal–organic framework for selective and sensitive detection of hydrazine and hydrogen peroxide, J. Environ. Chem. Eng. 9 (2021) 105182, https://doi.org/10.1016/j.jece.2021.105182.
[32] F. Salman, A. Zengin, H. Çelik Kazici, Synthesis and characterization of Fe3O4-supported metal–organic framework MIL-101(Fe) for a highly selective and sensitive hydrogen peroxide electrochemical sensor, Ionics 26 (2020) 5221–5232, https://doi.org/10.1007/s11581-020-03601-w.
[33] X. Luo, R. Abazari, M. Tahir, W.K. Fan, A. Kumar, T. Kalhorizadeh, A.M. Kirillov, A. R. Amani-Ghadim, J. Chen, Y. Zhou, Trimetallic metal–organic frameworks and derived materials for environmental remediation and electrochemical energy storage and conversion, Coord. Chem. Rev. 461 (2022) 214505, https://doi.org/10.1016/j.ccr.2022.214505.
[34] S. eun Kim, A. Muthurasu, Highly oriented nitrogen-doped carbon nanotube integrated bimetallic cobalt copper organic framework for non-enzymatic electrochemical glucose and hydrogen peroxide sensor, Electroanalysis 33 (2021) 1333–1345, https://doi.org/10.1002/elan.202060566.
[35] V. Archana, Y. Xia, R. Fang, G. Gnana kumar, Hierarchical CuO/NiO-carbon nanocomposite derived from metal organic framework on cello tape for the flexible and high performance nonenzymatic electrochemical glucose sensors, ACS Sustain. Chem. Eng. 7 (2019) 6707–6719, https://doi.org/10.1021/acssuschemeng.8b05980.
[36] D. Manoj, K. Theyagarajan, D. Saravanakumar, S. Senthilkumar, K. Thenmozhi, Aldehyde functionalized ionic liquid on electrochemically reduced graphene oxide as a versatile platform for covalent immobilization of biomolecules and biosensing, Biosens. Bioelectron. 103 (2018) 104–112, https://doi.org/10.1016/j.bios.2017.12.030.
[37] M. Saraf, R. Rajak, S.M. Mobin, A fascinating multitasking Cu-MOF/rGO hybrid for high performance supercapacitors and highly sensitive and selective electrochemical nitrite sensors, J. Mater. Chem. A 4 (2016) 16432–16445, https://doi.org/10.1039/C6TA06470A.
[38] W. Zheng, Y. Liu, P. Yang, Y. Chen, J. Tao, J. Hu, P. Zhao, Carbon nanohorns enhanced electrochemical properties of Cu-based metal organic framework for ultrasensitive serum glucose sensing, J. Electroanal. Chem. 862 (2020) 114018, https://doi.org/10.1016/j.jelechem.2020.114018.
[39] A.D. Daud, H.N. Lim, I. Ibrahim, N.A. Endot, N.S.K. Gowthaman, Z.T. Jiang, K. E. Cordova, An effective metal-organic framework-based electrochemical non-enzymatic glucose sensor, J. Electroanal. Chem. 921 (2022) 116676, https://doi.org/10.1016/j.jelechem.2022.116676.
[40] X. Zhang, Y. Xu, B. Ye, An efficient electrochemical glucose sensor based on porous nickel-based metal organic framework/carbon nanotubes composite (Ni-MOF/CNTs), J. Alloy. Compd. 767 (2018) 651–656, https://doi.org/10.1016/j.jallcom.2018.07.175.
[41] A.M.P. Peedikakkal, I.H. Aljundi, Mixed-metal Cu-BTC metal–organic frameworks as a strong adsorbent for molecular hydrogen at low temperatures, ACS Omega 5 (2020) 28493–28499, https://doi.org/10.1021/acsomega.0c02810.
[42] J. Zhu, H. Wen, W. Han, J. Ma, F. Zhang, C. Liu, Enhanced carbon dioxide absorption capacity of Cu-BTC through the combination of Cu-g-C_3N_4 at room temperature, J. Nanopart. Res. 25 (2023) 168, https://doi.org/10.1007/s11051-023-05817-z.
[43] E. Zhou, Y. Zhang, Y. Li, X. He, Cu(II)-Based MOF immobilized on multiwalled carbon nanotubes: synthesis and application for nonenzymatic detection of hydrogen peroxide with high sensitivity, Electroanalysis 26 (2014) 2526–2533, https://doi.org/10.1002/elan.201400341.
[44] J. Dong, J. Zheng, J. Hou, P. Zhao, Y. Liang, J. Lei, X. Luo, C. Hou, D. Huo, Au nanoparticle/CoFc/metal–organic framework as enzyme-free dual-signal ratiometric electrochemical sensor for in-situ determination of cell-secreted H_2O_2, ACS Appl. Nano Mater. 6 (2023) 11630–11639, https://doi.org/10.1021/acsanm.3c01628.
[45] S.P. Selvam, M. Hansa, K. Yun, Simultaneous differential pulse voltammetric detection of uric acid and melatonin based on a self-assembled Au nanoparticle–MoS_2 nanoflake sensing platform, Sens. Actuators B Chem. 307 (2020) 127683, https://doi.org/10.1016/j.snb.2020.127683.
[46] X. Shang, K.-L. Yan, Y. Rao, B. Dong, J.-Q. Chi, Y.-R. Liu, X. Li, Y.-M. Chai, C.-G. Liu, In situ cathodic activation of V-incorporated Ni_xS_y nanowires for enhanced hydrogen evolution, Nanoscale 9 (2017) 12353–12363, https://doi.org/10.1039/C7NR02867A.
[47] X. Shi, Y. Xie, L. Chen, J. Lu, L. Zhang, D. Sun, Combining quasi-ZIF-67 hybrid nanozyme and G-quadruplex/hemin DNAzyme for highly sensitive electrochemical sensing, Bioelectrochemistry 149 (2023) 108278, https://doi.org/10.1016/j.bioelechem.2022.108278.
[48] B. Huang, Y. Wang, Z. Lu, H. Du, J. Ye, One pot synthesis of palladium-cobalt nanoparticles over carbon nanotubes as a sensitive non-enzymatic sensor for glucose and hydrogen peroxide detection, Sens. Actuators B Chem. 252 (2017) 1016–1025, https://doi.org/10.1016/j.snb.2017.06.038.
[49] Y. Zhang, X. Wei, Q. Gu, J. Zhang, Y. Ding, L. Xue, M. Chen, J. Wang, S. Wu, X. Yang, S. Zhang, T. Lei, Q. Wu, Cascade amplification based on PEI-functionalized metal–organic framework supported gold nanoparticles/nitrogen–doped graphene quantum dots for amperometric biosensing applications, Electrochim. Acta 405 (2022) 139803, https://doi.org/10.1016/j.electacta.2021.139803.
[50] A. Portorreal-Bottier, S. Gutiérrez-Tarriño, J.J. Calvente, R. Andreu, E. Roldán, P. Oña-Burgos, J.L. Olloqui-Sariego, Enzyme-like activity of cobalt-MOF nanosheets for hydrogen peroxide electrochemical sensing, Sens. Actuators B Chem. 368 (2022) 132129, https://doi.org/10.1016/j.snb.2022.132129.
[51] H. Yao, W. Zhang, T. Yan, X. Li, X. Wang, Electrochemical sensor for detection of hydrogen peroxide based on Cu-doped ZIF-8 material modified with Chitosan and Cytochrome C, Int. J. Electrochem. Sci. 17 (2022) 220654, https://doi.org/10.20964/2022.06.68.
[52] B.T. Subramanian, S. Thomas, M.B. Gumpu, V.M.N. Biju, Aromatic carboxylic acid derived bimetallic nickel/cobalt electrocatalysts for oxygen evolution reaction and hydrogen peroxide sensing applications, J. Electroanal. Chem. 925 (2022) 116904, https://doi.org/10.1016/j.jelechem.2022.116904.
[53] W. Ling, Y. Hao, H. Wang, H. Xu, X. Huang, A novel Cu-metal-organic framework with two-dimensional layered topology for electrochemical detection using flexible sensors, Nanotechnology 30 (2019) 424002, https://doi.org/10.1088/1361-6528/ab30b6.
[54] H. Cui, S. Cui, S. Zhang, Q. Tian, Y. Liu, P. Zhang, M. Wang, J. Zhang, X. Li, Cu–MOF/hemin: a bionic enzyme with excellent dispersity for the determination of hydrogen peroxide released from living cells, Analyst 146 (2021) 5951–5961, https://doi.org/10.1039/D1AN01323H.
[55] C. Zhang, H. Yin, X. Bai, Z. Yang, Ru doping induced lattice distortion of Cu nanoparticles for boosting electrochemical nonenzymatic hydrogen peroxide sensing, Colloids Surf. Physicochem. Eng. Asp. 666 (2023) 131311, https://doi.org/10.1016/j.colsurfa.2023.131311.
[56] N.S. Lopa, Md.M. Rahman, F. Ahmed, S. Chandra Sutradhar, T. Ryu, W. Kim, A base-stable metal-organic framework for sensitive and non-enzymatic electrochemical detection of hydrogen peroxide, Electrochim. Acta 274 (2018) 49–56, https://doi.org/10.1016/j.electacta.2018.03.148.
[57] H. Mei, J. Xie, Z. Li, C. Lou, G. Lei, X. Liu, J. Zhang, Rational design of ZnO@ZIF-8 nanoarrays for improved electrochemical detection of H_2O_2, CrystEngComm 24 (2022) 1645–1654, https://doi.org/10.1039/D1CE01704G.
[58] J. Ma, W. Bai, J. Zheng, Non-enzymatic electrochemical hydrogen peroxide sensing using a nanocomposite prepared from silver nanoparticles and copper (II)-porphyrin derived metal-organic framework nanosheets, Microchim. Acta 186 (2019) 482, https://doi.org/10.1007/s00604-019-3551-1.
[59] M.-Q. Wang, Y. Zhang, S.-J. Bao, Y.-N. Yu, C. Ye, Ni(II)-based metal-organic framework anchored on carbon nanotubes for highly sensitive non-enzymatic hydrogen peroxide sensing, Electrochim. Acta 190 (2016) 365–370, https://doi.org/10.1016/j.electacta.2015.12.199.
[60] M. Ramesh, S. Umamatheswari, P.M. Vivek, C. Sankar, R. Jayavel, Synthesis of silver-bismuth oxide encapsulated hydrazone functionalized chitosan ($AgBi_2O_3$/FCS) nanocomposite for electrochemical sensing of glucose, H_2O_2 and Escherichia coli O157:H7, Int. J. Biol. Macromol. 264 (2024) 130533, https://doi.org/10.1016/j.ijbiomac.2024.130533.
[61] W. Wang, H. Tang, Y. Wu, Y. Zhang, Z. Li, Highly electrocatalytic biosensor based on Hemin@AuNPs/reduced graphene oxide/chitosan nanohybrids for non-enzymatic ultrasensitive detection of hydrogen peroxide in living cells, Biosens. Bioelectron. 132 (2019) 217–223, https://doi.org/10.1016/j.bios.2019.02.039.
[62] D. Sun, D. Yang, P. Wei, B. Liu, Z. Chen, L. Zhang, J. Lu, One-step electrodeposition of silver nanostructures on 2D/3D metal–organic framework ZIF-67: comparison and application in electrochemical detection of hydrogen peroxide, ACS Appl. Mater. Interfaces 12 (2020) 41960–41968, https://doi.org/10.1021/acsami.0c11269.
[63] Y. Xie, X. Shi, L. Chen, J. Lu, X. Lu, D. Sun, L. Zhang, Direct electrodeposition of bimetallic nanostructures on Co-based MOFs for electrochemical sensing of hydrogen peroxide, Front. Chem. 10 (2022), https://doi.org/10.3389/fchem.2022.856003.